Deep Resources Engineering 2 (2025) 100167

Contents lists available at ScienceDirect

Deep Resources Engineering

journal homepage: www.keaipublishing.com/en/journals/deepre/

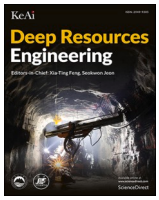

Full Length Article

# Metaheuristic multi-objective optimization-based microseismic source location approach with anisotropic P-wave velocity field

Xin Yin [a], Feng Gao [b,c], Honggan Yu [d,*], Yucong Pan [d,*], Quansheng Liu [d], He Liu [d,e]

[a] Department of Architecture and Civil Engineering, City University of Hong Kong, Tat Chee Avenue, Kowloon, Hong Kong, China
[b] Research Institute of Mine Construction, Tiandi Science and Technology Company Limited, Beijing 100013, China
[c] State Key Laboratory of Intelligent Coal Mining and Strata Control, Beijing 100013, China
[d] School of Civil Engineering, Wuhan University, Wuhan 430072, China
[e] School of Resource Environment and Safety Engineering, University of South China, Hengyang 421001, China

ARTICLE INFO

*Keywords:*
Underground engineering
Microseismic monitoring
Microseismic source location
P-wave velocity anisotropy
Metaheuristic multi-objective optimization

ABSTRACT

Rockburst is a common dynamic geological hazard, frequently occurring in underground engineering (e.g., TBM tunnelling and deep mining). In order to achieve rockburst monitoring and warning, the microseismic monitoring technique has been widely used in the field. However, the microseismic source location has always been a challenge, playing a vital role in the precise prevention and control of rockburst. To this end, this study proposes a novel microseismic source location model that considers the anisotropy of P-wave velocity. On the one hand, it assigns a unique P-wave velocity to each propagation path, abandoning the assumption of a homogeneous velocity field. On the other hand, it treats the P-wave velocity as a co-inversion parameter along with the source location, avoiding the predetermination of P-wave velocity. To solve this model, three various metaheuristic multi-objective optimization algorithms are integrated with it, including the whale optimization algorithm, the butterfly optimization algorithm, and the sparrow search algorithm. To demonstrate the advantages of the model in terms of localization accuracy, localization efficiency, and solution stability, four blasting cases are collected from a water diversion tunnel project in Xinjiang, China. Finally, the effect of the number of involved sensors on the microseismic source location is discussed.

## 1. Introduction

Rockburst is a common geological hazard in tunneling and mining activities [1,27,29,36–39,4,42,44,5]. It is characterized by suddenness, randomness, and impact, and poses significant threats to both workers and equipment [20,31,32,35]. Microseismic monitoring is a real-time in-situ three-dimensional monitoring technology for rock fractures [33,34]. It is known for the simplicity, high precision, and wide coverage, and has been popularly used for rockburst early warning [41]. Microseismic source location is crucial for analyzing the temporal-spatial evolution of microseismic events, providing a basis for identifying the potential rockburst region [25]. Additionally, the inversion of microseismic source parameters must consider the propagation path and attenuation of stress waves from the source to the sensors [28]. Thereby, accurate microseismic source location is a critical prerequisite for conducting rockburst early warning based on microseismic monitoring technology.

In theory, the localization of microseismic sources is achieved based on the arrival times, wave velocity, and sensor coordinates, as illustrated in Fig. 1 [43]. Depending on the type of the chosen wave velocity, microseismic source localization models can be categorized into two classes: the velocity-uniform model and the velocity-zoned model. The velocity-uniform model assumes a constant wave velocity in the rock mass, and is frequently used in non-layered media [8]. To minimize the localization error caused by inaccurate velocity measurements, the wave velocity is often eliminated during the application of the velocity-uniform model. For example, Dong et al. [9] proposed three velocity-uniform models, which separately used the arrival time, arrival time difference, and arrival time difference ratio as the dependent variable, to eliminate the need for pre-measured velocities, and these models were verified using blasting events from the Dongguashan copper mine. Besides the elimination method mentioned above, another commonly used approach is to solve for both the wave velocity and source location simultaneously by treating them as the co-variables in

* Corresponding authors.
*E-mail addresses:* yuhonggan@whu.edu.cn (H. Yu), pyc1991@whu.edu.cn (Y. Pan).

https://doi.org/10.1016/j.deepre.2025.100167
Received 13 January 2025; Received in revised form 11 February 2025; Accepted 13 February 2025
Available online 14 February 2025

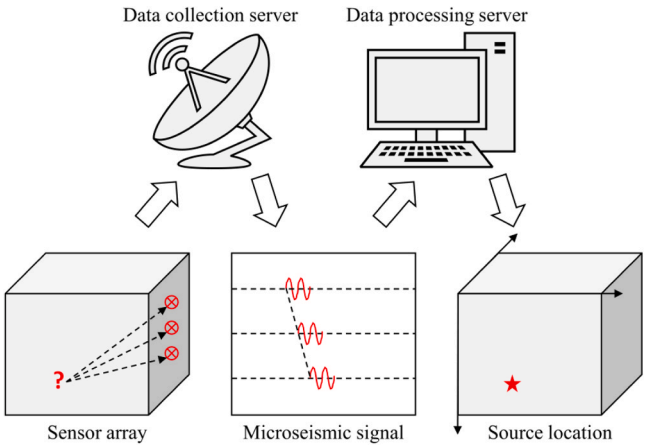


**Fig. 1.** Basic principle of microseismic source location.

the objective function. For example, Li et al. [19] developed a velocity-uniform model based on the virtual field optimization method, where the wave velocity was treated as an inversion parameter without prior measurement, and this model was applied to the Kaiyang phosphate mine. The velocity-zoned model divides the rock mass into different sections, with the wave velocity assumed to be constant within the same section but varying between sections [14]. This model is typically used in layered media. For example, Gong et al. [13] devised a velocity-zoned model based on the shortest propagation path and validated it in a coal-rock layered system in a coal mine. Similarly, Dai et al. [7] invented a velocity-zoned model based on the minimum travel time and applied it to the layered rock slope on the left bank of the Baihetan hydropower station.

In addition to the localization model, the design of the solution algorithm also significantly impacts the accuracy of microseismic source localization [10,22]. Based on the solving principles, these algorithms can be divided into two categories: non-iterative and iterative methods [2]. Non-iterative methods transform nonlinear problems into linear ones for solving, offering the simplicity in the solving process but potentially resulting in multiple solutions. To ensure the uniqueness of the solution, non-iterative methods require the number of sensors to be no fewer than the number of parameters to be solved. Classic non-iterative methods include USBM [16,17] and INGLADA [15]. Iterative methods, on the other hand, continuously approach the optimal solution through iterative calculations. Compared to non-iterative methods, iterative methods offer better resistance to interference and have stronger robustness. The earliest iterative method used for microseismic source localization was proposed by Geiger [11], which updates the initial solution through a tangent-based derivative approach until the residual function of the arrival time difference converges to a minimum. Buland [3] and Thurber [26] later improved upon the Geiger method [11], expanding the residual function of the arrival time difference using the first- or second-order Taylor expansion before applying iterative updates to the initial solution. However, these methods above require a suitable initial solution for convergence to the global minimum, and it may result in a singular matrix and terminate the iteration when the source is far from the sensors. To address these limitations, the Gauss-Newton method [6,24] and the simplex method [21,24] have been introduced into microseismic source localization. The Gauss-Newton method shares similarities with the improved Geiger method, as both express the objective function as a sum of Taylor series terms and error terms. The difference lies in the Gauss-Newton method's use of secant line approximation rather than tangent line approximation. However, both the Geiger method and the improved Geiger method, as well as the Gauss-Newton method and the simplex method, are heavily reliant on the coefficient matrix of the localization model. As a result, these methods are typically more effective for microseismic sources within sensor arrays, but less effective for those outside the array.

This study proposes a microseismic source localization model that considers the anisotropic wave velocity to address the challenges posed by inhomogeneity in the rock. In this model, the wave velocity is treated as a co-inversion parameter with the source location, helping to mitigate the problem of inaccurate velocity measurements. Additionally, to achieve efficient and accurate inversion of the large-scale parameters in the proposed localization model, three solution schemes are designed based on three metaheuristic multi-objective optimization algorithms, including whale optimization, butterfly optimization, and sparrow search, which enhance global search capabilities while effectively reducing dependency on the coefficient matrix of the localization model. The organization of this paper is as follows: Section 2 describes the proposed framework for microseismic source location, Section 3 analyzes the location results and evaluates the location performance, Section 4 carries out some discussion, and Section 5 summarizes the main conclusions.

## 2. Metaheuristic velocity-anisotropic model for microseismic source location

### 2.1. Traditional microseismic source localization models

Based on the difference of inversion parameters, traditional microseismic source localization models can be categorized into three classes: (1) Position (Source position)-Time (Origin time) joint inversion-based location model (PTLM); (2) Position (Source position)-Velocity (Wave velocity) joint inversion-based location model (PVLM); (3) Position (Source position) inversion-based location model (PLM) [18]. The basic principles of these three traditional models are introduced as follows:

(1) PTLM

PTLM is proposed based on the travel time residual theory. PTLM assumes that "the difference between the P-wave arrival time recorded by the sensor and the origin time of the microseismic event" is equal to "the travel time of the P-wave from the microseismic source to the sensor." Therefore, the objective function $f(x_0, y_0, z_0, t_0)$ is constructed as:

$$f(x_0, y_0, z_0, t_0) = \sum_{i=1}^{n} \left( t_i - t_0 - \frac{l_i}{v} \right)^2 \tag{1}$$

where, $(x_0, y_0, z_0)$ is the microseismic source location; $t_0$ is the origin time of the microseismic event; $v$ is the wave velocity; $n$ is the number of sensors; $t_i$ is the P-wave arrival time recorded by the $i$-th sensor; $l_i$ is the distance from the microseismic source to the $i$-th sensor, calculated as:

$$l_i = \sqrt{(x_i - x_0)^2 + (y_i - y_0)^2 + (z_i - z_0)^2} \tag{2}$$

where, $(x_i, y_i, z_i)$ is the location of the $i$-th sensor.

By minimizing the objective function, the source location and origin time can be inverted. When using PTLM for microseismic source localization, it is necessary to pre-determine the wave velocity in the rock mass. If the measured wave velocity differs from the actual wave velocity, it will significantly affect the localization accuracy.

(2) PVLM

Similar to PTLM, PVLM is also based on the travel time residual theory. PVLM assumes that "the difference in P-wave arrival times recorded by two sensors" is equal to "the difference in travel times of the P-wave from the microseismic source to these two sensors." Therefore, the objective function $f(x_0, y_0, z_0, v)$ is constructed as:

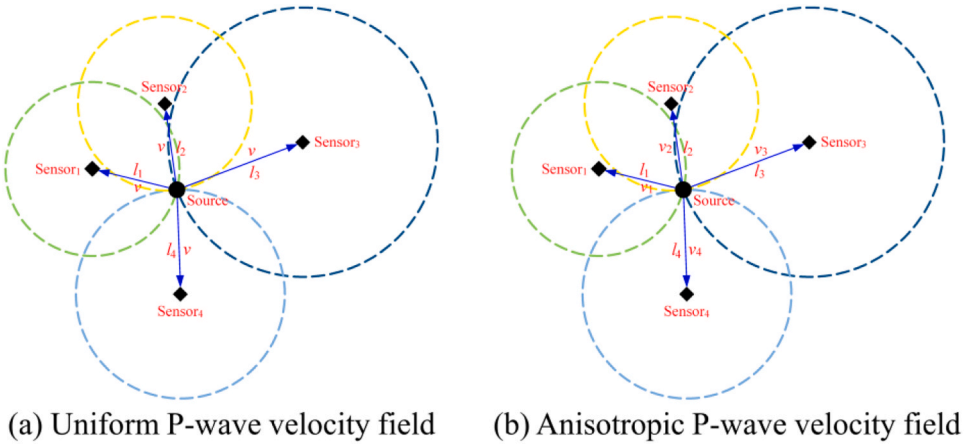


**Fig. 2.** Microseismic source location model.

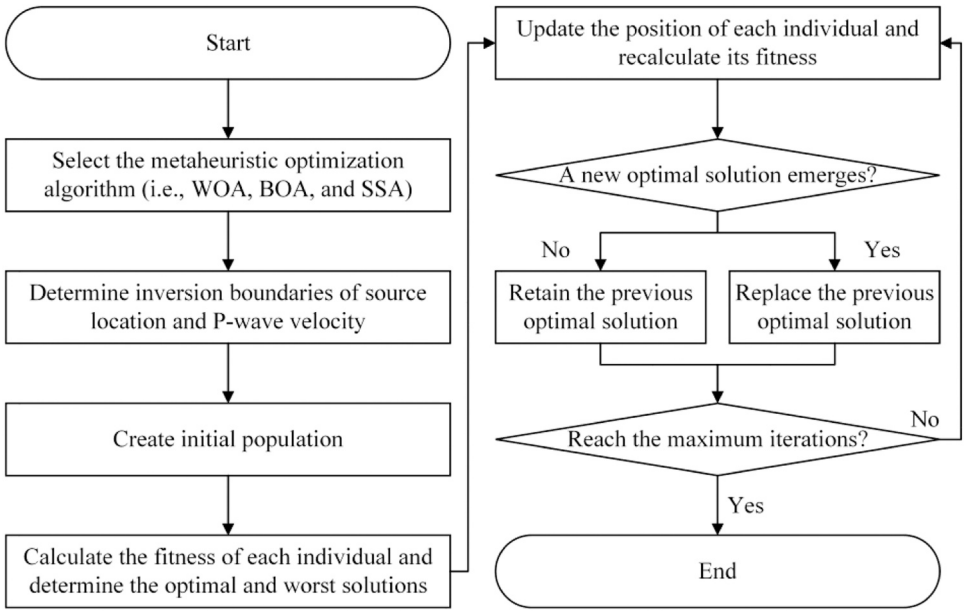


**Fig. 3.** Solving procedure of microseismic source location model.

**Table 1**
Blasting coordinates of four blasting cases.

| Blasting case | Blasting coordinate | | |
|---|---|---|---|
| | $x$/m | $y$/m | $z$/m |
| #1 | 4889407.643 | 500923.754 | 1404.804 |
| #2 | 4889285.482 | 500898.607 | 1391.814 |
| #3 | 4889241.905 | 500892.570 | 1386.412 |
| #4 | 4889136.181 | 500872.308 | 1374.392 |

$$f(x_0, y_0, z_0, v) = \sum_{i,j=1,i\neq j}^{n} \left( t_i - t_j - \frac{l_i - l_j}{v} \right)^2 \tag{3}$$

where, $(x_0, y_0, z_0)$ is the microseismic source location; $v$ is the wave velocity; $n$ is the number of sensors; $t_i$ and $t_j$ are the P-wave arrival times recorded by the $i$-th and $j$-th sensors, respectively; $l_i$ and $l_j$ are the distances from the microseismic source to the $i$-th and $j$-th sensors, respectively.

PVLM processes the wave velocity as a co-inversion parameter with the source location, eliminating the need for pre-determined wave velocity. By minimizing the objective function, both the source location and wave velocity can be simultaneously determined.

(3) PLM

To reduce the number of inversion parameters, PLM no longer relies on the travel time residual theory. PLM assumes that "the P-wave velocities along different propagation paths are the same." Therefore, the objective function $f(x_0, y_0, z_0)$ is constructed as:

$$f(x_0, y_0, z_0) = \sum_{i,j,k=1,i\neq j\neq k}^{n} \left( \frac{l_i - l_j}{t_i - t_j} - \frac{l_i - l_k}{t_i - t_k} \right)^2 \tag{4}$$

where, $(x_0, y_0, z_0)$ is the microseismic source location; $n$ is the number of sensors; $t_i$, $t_j$, and $t_k$ are the P-wave arrival times recorded by the $i$-th, $j$-th, and $k$-th sensors, respectively; $l_i$, $l_j$, and $l_k$ are the distances from the microseismic source to the $i$-th, $j$-th, and $k$-th sensors, respectively.

In PLM, the source location is the only inversion parameter, as neither the origin time nor the wave velocity is treated as co-inversion parameters, thereby reducing the inversion load.

Based on the above analysis, it can be observed that PTLM, PVLM, and PLM treat the rock mass as a homogeneous medium, assuming that

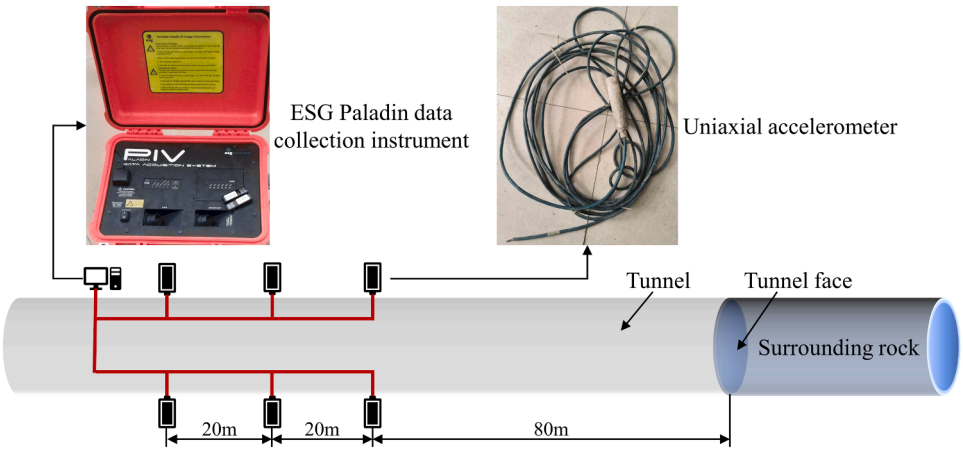


**Fig. 4.** Microseismic monitoring scheme.

**Table 2**
Sensor coordinates for four blasting cases.

| Blasting case | Sensor coordinate | Sensor number | | | | | |
|---|---|---|---|---|---|---|---|
| | | 1 | 2 | 3 | 4 | 5 | 6 |
| #1 | x/m | 4889485.949 | 4889485.573 | 4889505.198 | 4889505.132 | 4889525.08 | 4889525.33 |
| | y/m | 500933.701 | 500926.279 | 500936.556 | 500929.09 | 500939.957 | 500931.994 |
| | z/m | 1417.091 | 1417.062 | 1419.437 | 1419.541 | 1422.553 | 1421.684 |
| #2 | x/m | 4889366.442 | 4889366.901 | 4889386.589 | 4889386.961 | 4889406.045 | 4889406.99 |
| | y/m | 500912.004 | 500904.981 | 500914.358 | 500907.329 | 500917.772 | 500910.518 |
| | z/m | 1401.7 | 1401.768 | 1402.947 | 1403.177 | 1405.301 | 1405.423 |
| #3 | x/m | 4889322.658 | 4889323 | 4889341.985 | 4889342.17 | 4889361.199 | 4889361.29 |
| | y/m | 500903.359 | 500896.285 | 500905.176 | 500897.785 | 500908.396 | 500900.145 |
| | z/m | 1398.582 | 1398.616 | 1400.293 | 1399.855 | 1401.148 | 1401.127 |
| #4 | x/m | 4889218.185 | 4889218.071 | 4889238.504 | 4889238.512 | 4889258.573 | 4889258.077 |
| | y/m | 500887.215 | 500880.292 | 500889.56 | 500882.536 | 500891.927 | 500884.61 |
| | z/m | 1386.222 | 1386.342 | 1387.263 | 1387.946 | 1389.705 | 1389.639 |

the wave velocity in the rock mass is a constant, as shown in Fig. 2(a). However, in real engineering applications, rock masses are heterogeneous, meaning that the wave velocity exhibits anisotropy. Moreover, the propagation paths of waves from the microseismic source to different sensors are inevitably different. In such cases, a constant wave velocity for modeling is clearly unreasonable. Thus, this study proposes the velocity anisotropy-based location model (VALM) to improve the accuracy of microseismic source localization.

### 2.2. Microseismic source location model with velocity anisotropy

VALM assigns a unique wave velocity to each propagation path, as shown in Fig. 2(b). To avoid the influence of wave velocity measurement errors on the localization accuracy, VALM treats both the wave velocity and source location as the co-inversion parameters.

It is assumed that the microseismic monitoring system has $n$ sensors, and the wave velocities from the source to varying sensor are denoted as $v_1, v_2, \ldots, v_n$. The travel time $\Delta t_i$ of the P-wave from the source to the $i$-th sensor can be calculated as:

$$\Delta t_i = \frac{l_i}{v_i} \tag{5}$$

where, $l_i$ and $v_i$ are the distance and wave velocity from the source to the $i$-th sensor, respectively.

Similarly, the travel time $\Delta t_j$ of the P-wave from the source to the $j$-th sensor is calculated as:

$$\Delta t_j = \frac{l_j}{v_j} \tag{6}$$

where, $l_j$ and $v_j$ are the distance and wave velocity from the source to the $j$-th sensor, respectively.

In principle, the difference in the travel times of the P-wave from the source to the $i$-th and $j$-th sensors should equal the difference in the arrival times of the P-wave recorded by these two sensors, which is,

$$\frac{l_i}{v_i} - \frac{l_j}{v_j} = t_i - t_j \tag{7}$$

where, $t_i$ and $t_j$ are the P-wave arrival times recorded by the $i$-th and $j$-th sensors, respectively.

Based on this, the objective function $f(x_0, y_0, z_0, v_1, v_2, \ldots, v_n)$ is constructed as follows:

$$f(x_0, y_0, z_0, v_1, v_2, \ldots, v_n) = \sum_{i,j=1, i\neq j}^{n} \left[ (t_i - t_j) - \left( \frac{l_i}{v_i} - \frac{l_j}{v_j} \right) \right]^2 \tag{8}$$

$$l_i = \sqrt{(x_i - x_0)^2 + (y_i - y_0)^2 + (z_i - z_0)^2} \tag{9}$$

$$l_j = \sqrt{(x_j - x_0)^2 + (y_j - y_0)^2 + (z_j - z_0)^2} \tag{10}$$

where, $(x_0, y_0, z_0)$ is the source location; $(x_i, y_i, z_i)$ and $(x_j, y_j, z_j)$ are the locations of the $i$-th and $j$-th sensors, respectively.

Finally, the source location can be determined by minimizing the above objective function, namely:

$$\min\left(f(x_0, y_0, z_0, v_1, v_2, \ldots, v_n)\right) \tag{11}$$

VALM includes a total of $n + 3$ inversion parameters. Compared to

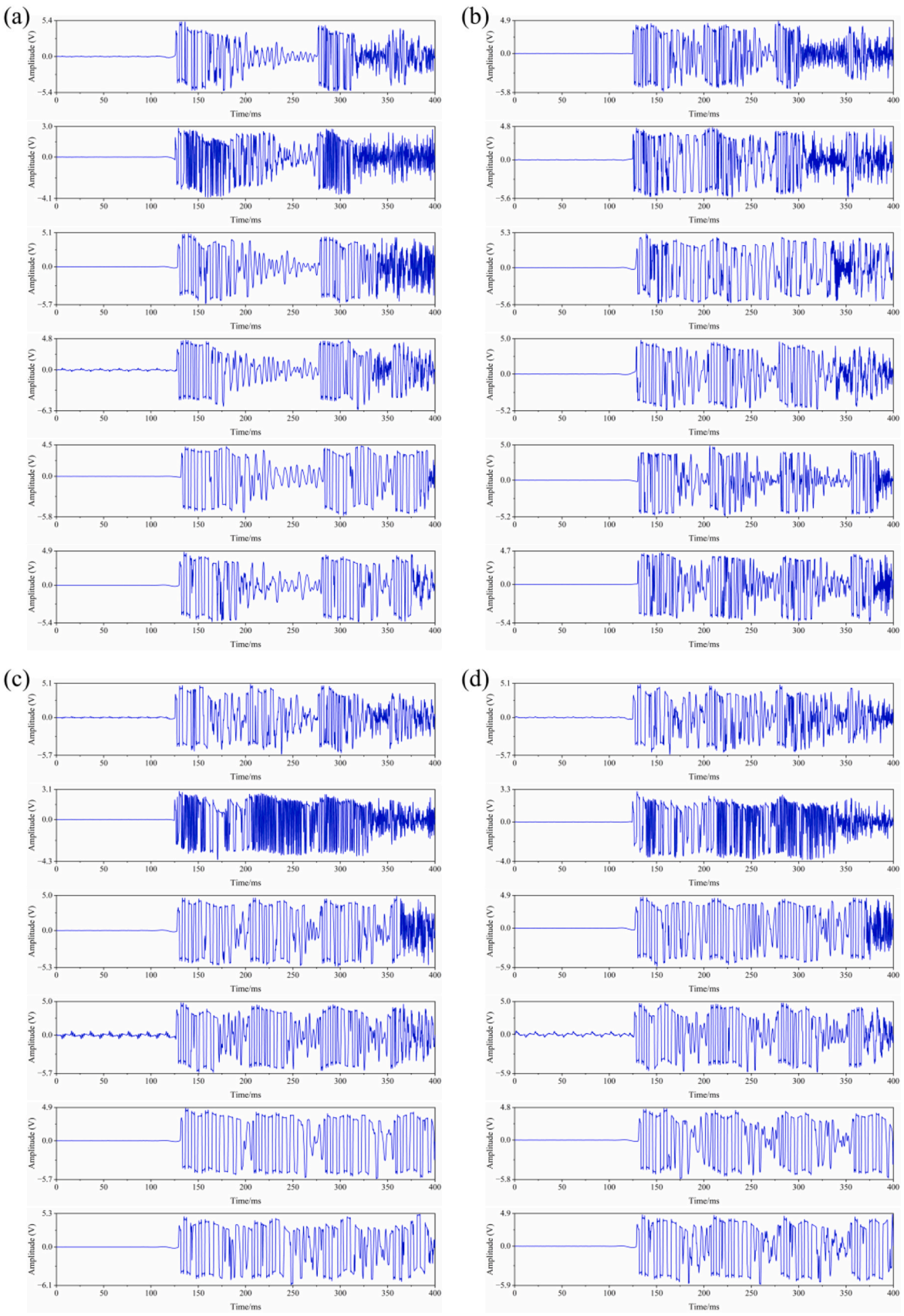


**Fig. 5.** Microseismic signals: (a) Blasting case #1; (b) Blasting case #2; (c) Blasting case #3; (d) Blasting case #4.

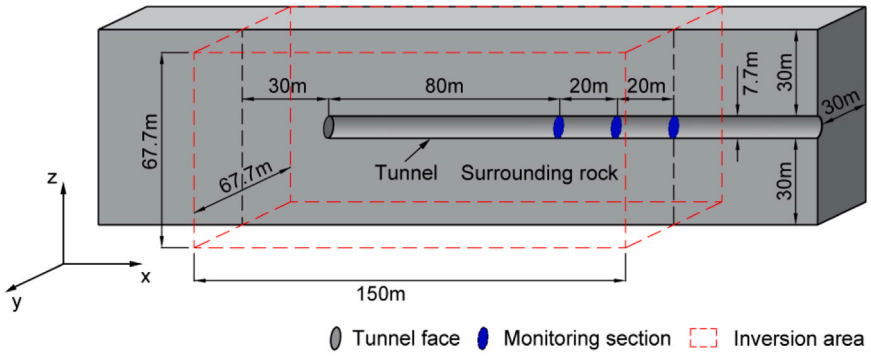


**Fig. 6.** Inversion area of microseismic source location. Note: The diameter of the tunnel is 7.7 m.

**Table 3**
Inversion boundaries for the source location in the four blasting cases.

| Inversion boundary | | Blasting case | | | |
|---|---|---|---|---|---|
| | | #1 | #2 | #3 | #4 |
| *x*/m | Upper | 4889525.205 | 4889406.518 | 4889361.245 | 4889258.325 |
| | Lower | 4889375.205 | 4889256.518 | 4889211.245 | 4889108.325 |
| *y*/m | Upper | 500951.608 | 500930.969 | 500924.230 | 500908.642 |
| | Lower | 500883.908 | 500863.269 | 500856.530 | 500840.942 |
| *z*/m | Upper | 1440.618 | 1428.286 | 1427.058 | 1413.403 |
| | Lower | 1372.918 | 1360.586 | 1359.358 | 1345.703 |

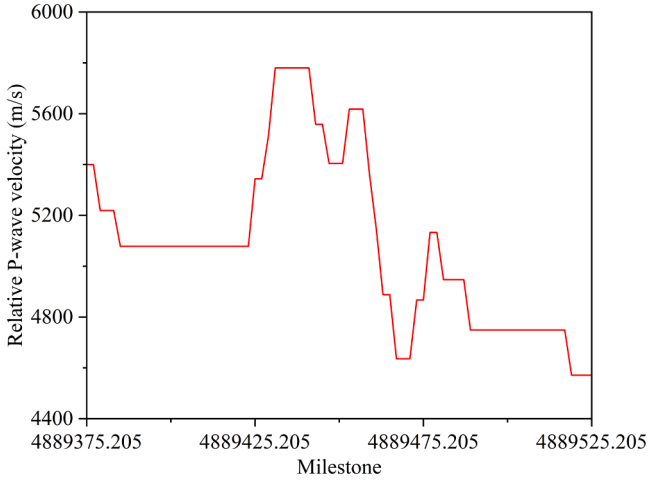


**Fig. 7.** Relative P-wave velocity measured by the TRT.

**Table 4**
Inversion boundaries for the P-wave velocity in the four blasting cases.

| Inversion boundary | | Blasting case | | | |
|---|---|---|---|---|---|
| | | #1 | #2 | #3 | #4 |
| *v*/m/s | Upper | 6095 | 6137 | 5989 | 6200 |
| | Lower | 4820 | 4774 | 4449 | 4729 |

PTLM, PVLM, and PLM, VALM has a larger number of inversion parameters. To achieve efficient and accurate inversion of these large-scale parameters, three different metaheuristic multi-objective optimization algorithms are employed for solving the problem.

### 2.3. Solving scheme with metaheuristic multi-objective optimization

#### 2.3.1. Whale optimization algorithm

Whale optimization algorithm (WOA) is a metaheuristic multi-objective optimization algorithm inspired by the hunting behavior of humpback whales [12]. Its search process is divided into two phases: Exploration and Exploitation. Exploration is a global search behavior used to locate the valuable region (i.e., prey) within the search space, while exploitation is a local search behavior that investigates the valuable region in more detail.

The mathematical model for the exploration phase is described as follows:

$$\vec{X}(t+1) = \overrightarrow{X_{rand}}(t) - A \cdot \left| C \cdot \overrightarrow{X_{rand}}(t) - \vec{X}(t) \right| \tag{12}$$

where, $t$ is the current iteration; $\overrightarrow{X_{rand}}$ is the position vector of a randomly chosen whale from the current population; $A$ and $C$ are coefficients calculated by Eqs. (13) and (14), respectively.

$$A = 2a \cdot r - a \tag{13}$$

$$C = 2 \cdot r \tag{14}$$

where, $a$ decreases linearly from 2 to 0 over the course of iterations; $r$ is a random number in the range [0,1].

Once the prey is found, the whale uses a bubble-net method to attack the prey, swimming in increasingly smaller circles along a spiral path around the prey. To mathematically model the exploitation phase, it is divided into two parts: Shrinking encircling prey (Eq. (15)) and Spiral updating position (Eq. (16)). And, it is assumed that whales have a 50 % probability of choosing between shrinking encircling prey and spiral updating position to simulate this synchronous behavior, as shown in Eq. (17).

$$\vec{X}(t+1) = \overrightarrow{X_{best}}(t) - A \cdot \left| C \cdot \overrightarrow{X_{best}}(t) - \vec{X}(t) \right| \tag{15}$$

$$\vec{X}(t+1) = \left| \overrightarrow{X_{best}}(t) - \vec{X}(t) \right| \cdot e^{bl} \cdot \cos(2\pi l) + \overrightarrow{X_{best}}(t) \tag{16}$$

$$\vec{X}(t+1) = \begin{cases} \overrightarrow{X_{best}}(t) - A \cdot \left| C \cdot \overrightarrow{X_{best}}(t) - \vec{X}(t) \right| & p < 0.5 \\ \left| \overrightarrow{X_{best}}(t) - \vec{X}(t) \right| \cdot e^{bl} \cdot \cos(2\pi l) + \overrightarrow{X_{best}}(t) & p \geq 0.5 \end{cases} \tag{17}$$

where, $\overrightarrow{X_{best}}$ is the position vector of the current global best solution; $b$ is a constant that defines the shape of the logarithmic spiral; $l$ is a random number in the range [-1, 1]; $p$ is a random number in the range [0,1].

#### 2.3.2. Butterfly optimization algorithm

Butterfly optimization algorithm (BOA) is a metaheuristic multi-objective optimization algorithm inspired by the foraging and mating behavior of butterflies [23]. In nature, butterflies use their sense of

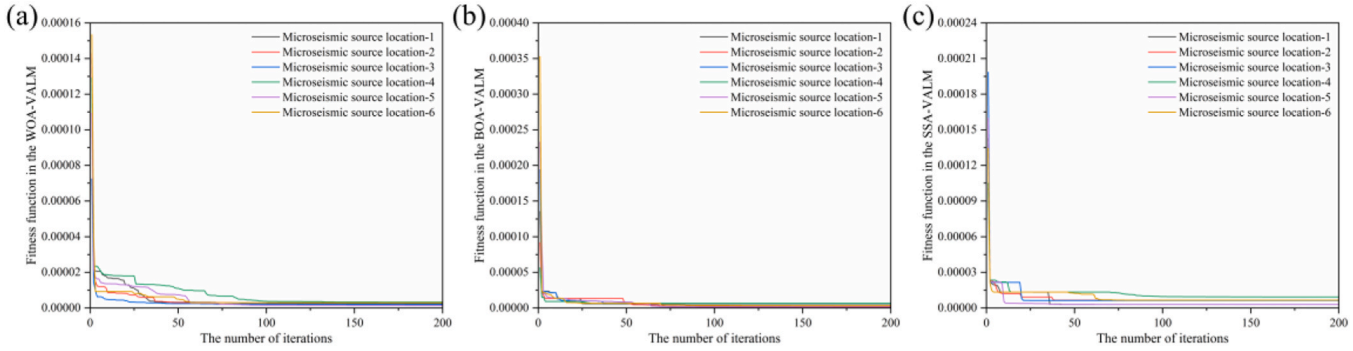


**Fig. 8.** Iterative process of microseismic source location for blasting case #1: (a) WOA-VALM; (b) BOA-VALM; (c) SSA-VALM.

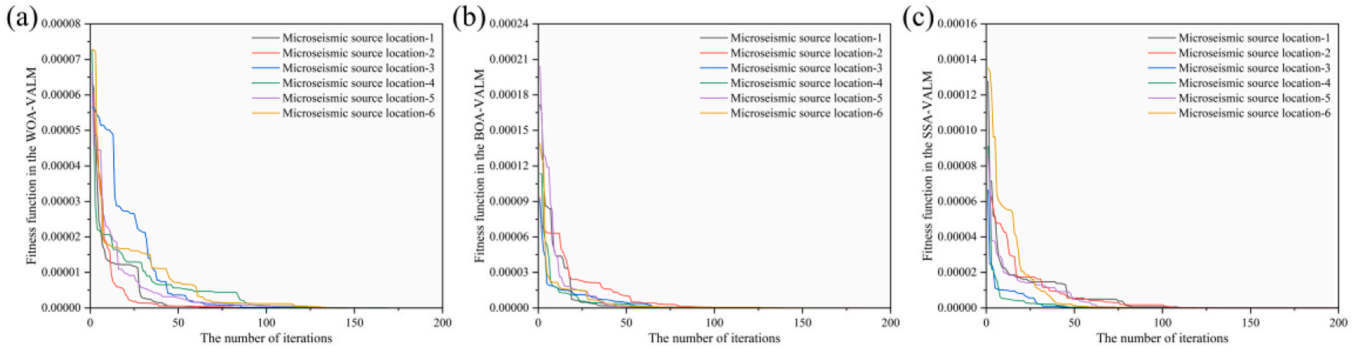


**Fig. 9.** Iterative process of microseismic source location for blasting case #2: (a) WOA-VALM; (b) BOA-VALM; (c) SSA-VALM.

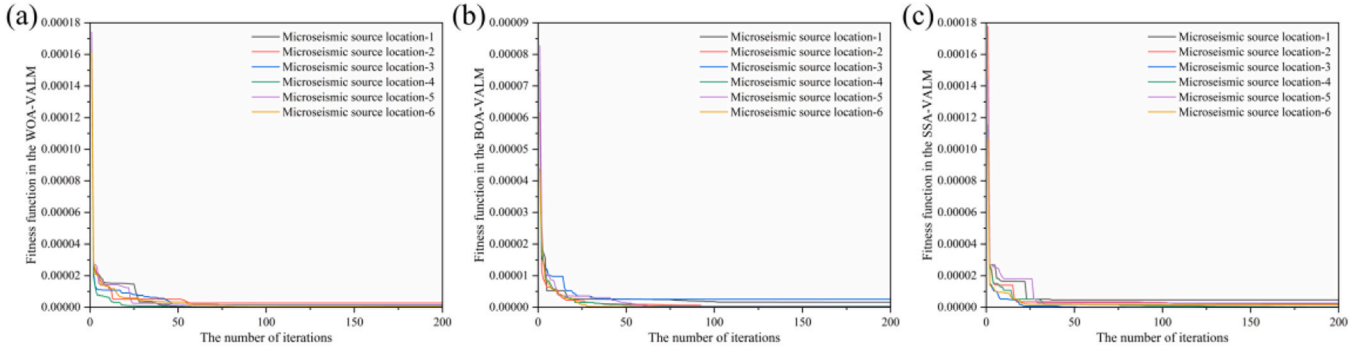


**Fig. 10.** Iterative process of microseismic source location for blasting case #3: (a) WOA-VALM; (b) BOA-VALM; (c) SSA-VALM.

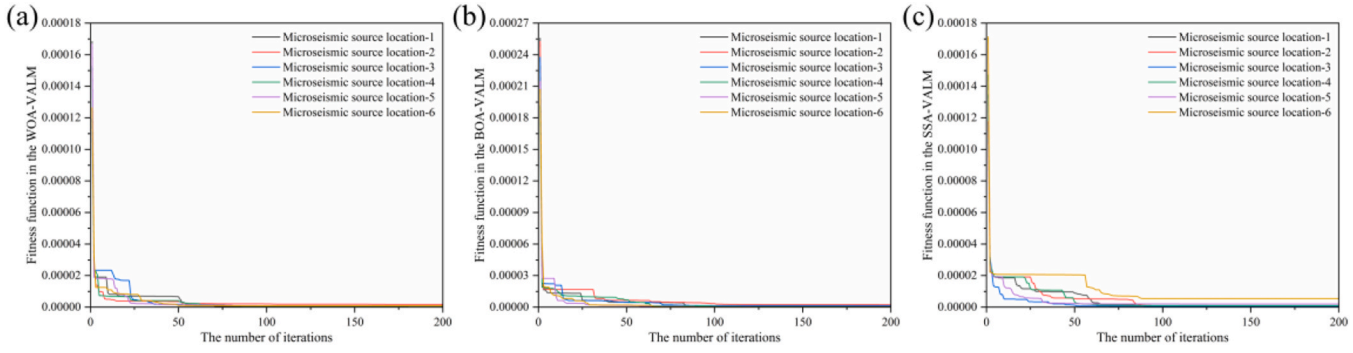


**Fig. 11.** Iterative process of microseismic source location for blasting case #4: (a) WOA-VALM; (b) BOA-VALM; (c) SSA-VALM.

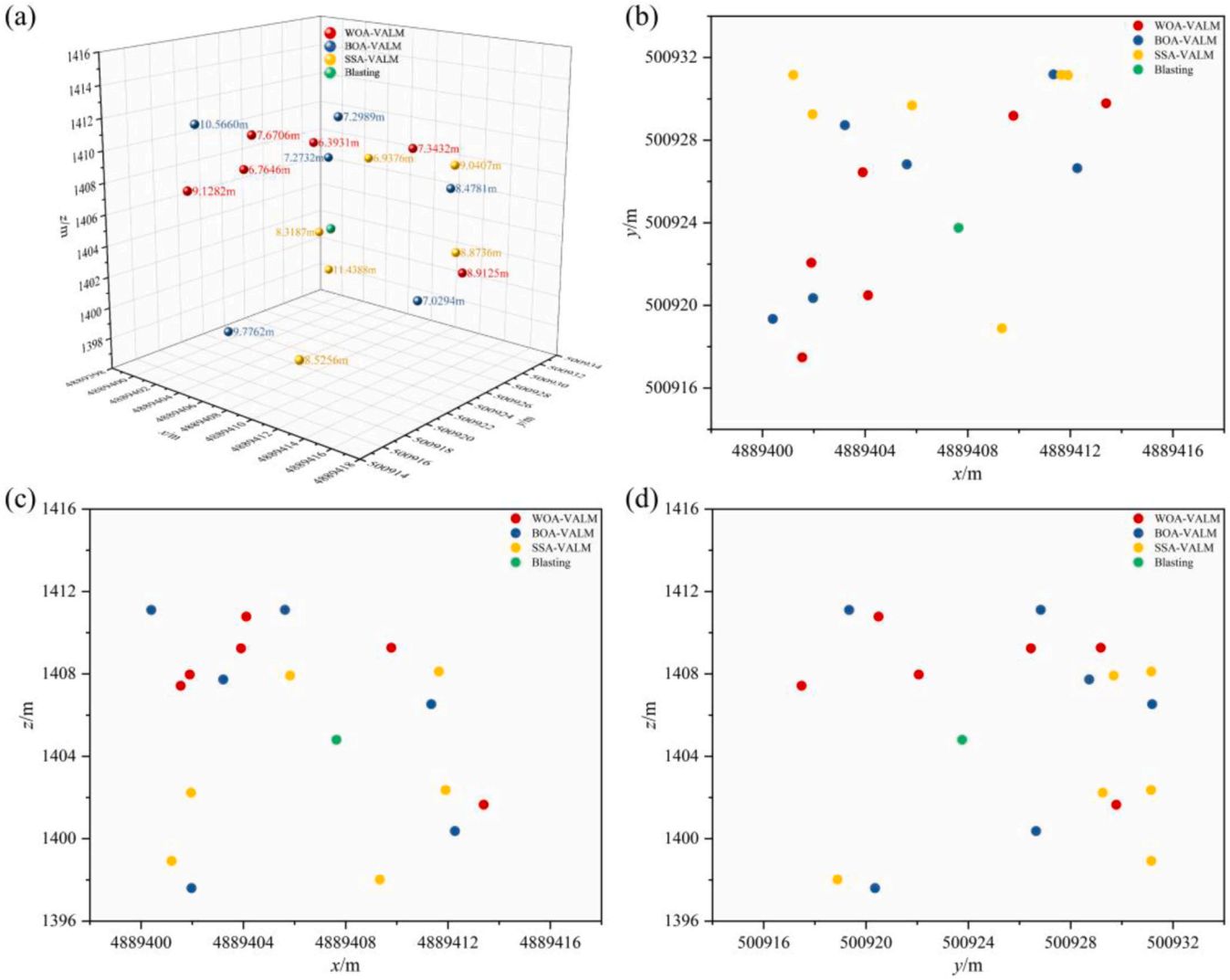


**Fig. 12.** Microseismic source location results for blasting case #1: (a) 3D visualization; (b) *x*-*y* plane projection; (c) *x*-*z* plane projection; (d) *y*-*z* plane projection. Numerical annotations in Fig. 12(a), such as 7.2989 m, represent location errors.

smell, sight, taste, touch, and hearing to find food and mates, with smell playing the most crucial role. Butterflies are highly accurate at locating the source of a scent and can differentiate between different scents and perceive their intensities.

In BOA, the scent is mathematically described as:

$$f = cI^a \tag{18}$$

where, $f$ is the perceived scent intensity; $c \in [0,1]$ is the sensory modality; $I$ is the stimulus intensity depicted by the fitness function; $a \in [0,1]$ is the power exponent.

When a butterfly or nectar emits a strong scent, nearby butterflies are attracted to it. This process represents the global search, and the butterfly's position is updated as according to Eq. (19):

$$x_i^{t+1} = x_i^t + \left(r^2 \cdot g^* - x_i^t\right) \cdot f_i \tag{19}$$

where, $t$ and $t+1$ are the iteration steps; $x_i$ is the position of the $i$-th butterfly; $g^*$ is the current global best solution; $f_i$ is the scent intensity of the $i$-th butterfly; $r$ is a random number in the range [0,1].

In contrast, when butterflies cannot sense any scent around them, they move randomly. This process can be viewed as the local search, where the butterfly positions are updated according to Eq. (20):

$$x_i^{t+1} = x_i^t + \left(r^2 \cdot x_j^t - x_k^t\right) \cdot f_i \tag{20}$$

where, $x_j$ and $x_k$ are the positions of the randomly selected $j$-th and $k$-th butterflies from the population, respectively.

### 2.3.3. Sparrow search algorithm

Sparrow search algorithm (SSA) is a metaheuristic multi-objective optimization algorithm inspired by the foraging and anti-predation behaviors of sparrows [30]. The sparrow population is divided into three groups: discoverers, followers, and sentinels, where:

(1) Discoverers are responsible for searching for food and providing foraging areas and directions for the followers. When predators appear, the discoverers must lead the followers to a safe zone.
(2) Some followers will compete with discoverers, and when a follower finds a better food source, it becomes a new discoverer, while the original discoverer becomes a follower. Other followers, driven by hunger, leave the discoverers and forage in other areas.
(3) Sentinels are sparrows with a heightened sense of danger, typically making up 10–20 % of the population. Sentinels on the edge of the population will move towards the center, while those in the

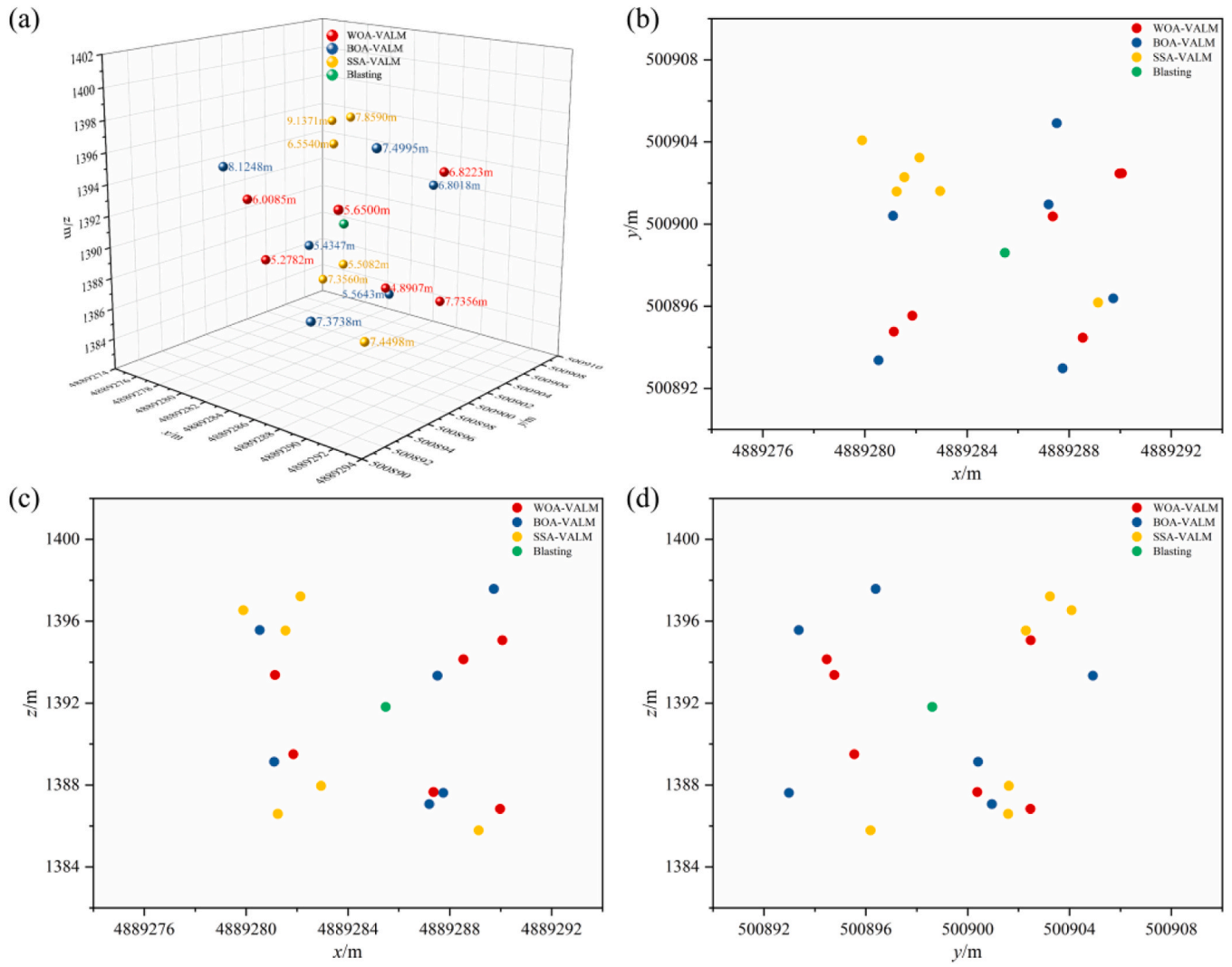


**Fig. 13.** Microseismic source location results for blasting case #2: (a) 3D visualization; (b) *x*-*y* plane projection; (c) *x*-*z* plane projection; (d) *y*-*z* plane projection. Numerical annotations in Fig. 13(a), such as 7.8590 m, represent location errors.

center will move towards other nearby sparrows to reduce their risk of predation.

The position update strategies for discoverers, followers, and sentinels differ. For discoverers, the position is updated using Eq. (21), where $R_2 < ST$ indicates that no predators are present in the surroundings, and $R_2 \geq ST$ indicates that predators are present in the surrounding area.

$$X_{ij}^{t+1} = \begin{cases} X_{ij}^{t} \cdot \exp(-i/(\alpha \cdot \boldsymbol{iter}_{\max})) & R_2 < ST \\ X_{ij}^{t} + Q \cdot L & R_2 \geq ST \end{cases} \tag{21}$$

where, $t$ is the current iteration; $X_{ij}$ is the $j$-th component of the position of the $i$-th sparrow; $\boldsymbol{iter}_{\max}$ is the maximum number of iterations; $\alpha$ is a random number in (0, 1]; $Q$ is a random number following a normal distribution; $L$ is a $1 \times d$ matrix with all elements set to 1; $R_2$ is the warning value; $ST$ is the safety threshold.

For followers, the position is updated using Eq. (22). To simulate the behavior of followers, it is assumed that the $i$-th ($i > n/2$) follower leaves the discoverer due to hunger and forages on its own.

$$X_{ij}^{t+1} = \begin{cases} Q \cdot \exp\left(\left(X_{\boldsymbol{worst},j}^{t} - X_{ij}^{t}\right)/i^2\right) & i > n/2 \\ X_{Pj}^{t+1} + \left|X_{ij}^{t} - X_{Pj}^{t+1}\right| \cdot A^{+} \cdot L & i \leq n/2 \end{cases} \tag{22}$$

where, $X_{Pj}$ is the $j$-th component of the best position among the discoverers; $X_{\boldsymbol{worst},j}$ is the $j$-th component of the worst position in the whole population; $n$ is the number of sparrow in the whole population; $A$ is a $1 \times d$ random matrix with elements assigned as 1 or $-1$ and $A^{+} = A^{T}\left(AA^{T}\right)^{-1}$.

For sentinels, the position is updated using Eq. (23), where $f_i > f_g$ indicates that the sentinel is located at the edge of the population, and $f_i = f_g$ indicates that the sentinel is located within the population.

$$X_{ij}^{t+1} = \begin{cases} X_{\boldsymbol{best},j}^{t} + \beta \cdot \left|X_{ij}^{t} - X_{\boldsymbol{best},j}^{t}\right| & f_i > f_g \\ X_{ij}^{t} + K \cdot \left(\left(X_{ij}^{t} - X_{\boldsymbol{worst},j}^{t}\right)/\left(f_i - f_w + \varepsilon\right)\right) & f_i = f_g \end{cases} \tag{23}$$

where, $X_{\boldsymbol{best},j}$ is the $j$-th component of the current global best solution; $f_g$, $f_w$, and $f_i$ are the values of the fitness function of the current global best solution, the current global worst solution, and the $i$-th sentinel, respectively; $K$ is a random number in the range [-1, 1]; $\beta$ is a random number following a normal distribution with a mean of 0 and variance of 1.

### 2.3.4. Solving procedure

The core idea of the solving scheme is to treat the objective function of the VALM (i.e., Eq. (11)) as the fitness function of the WOA, BOA, and

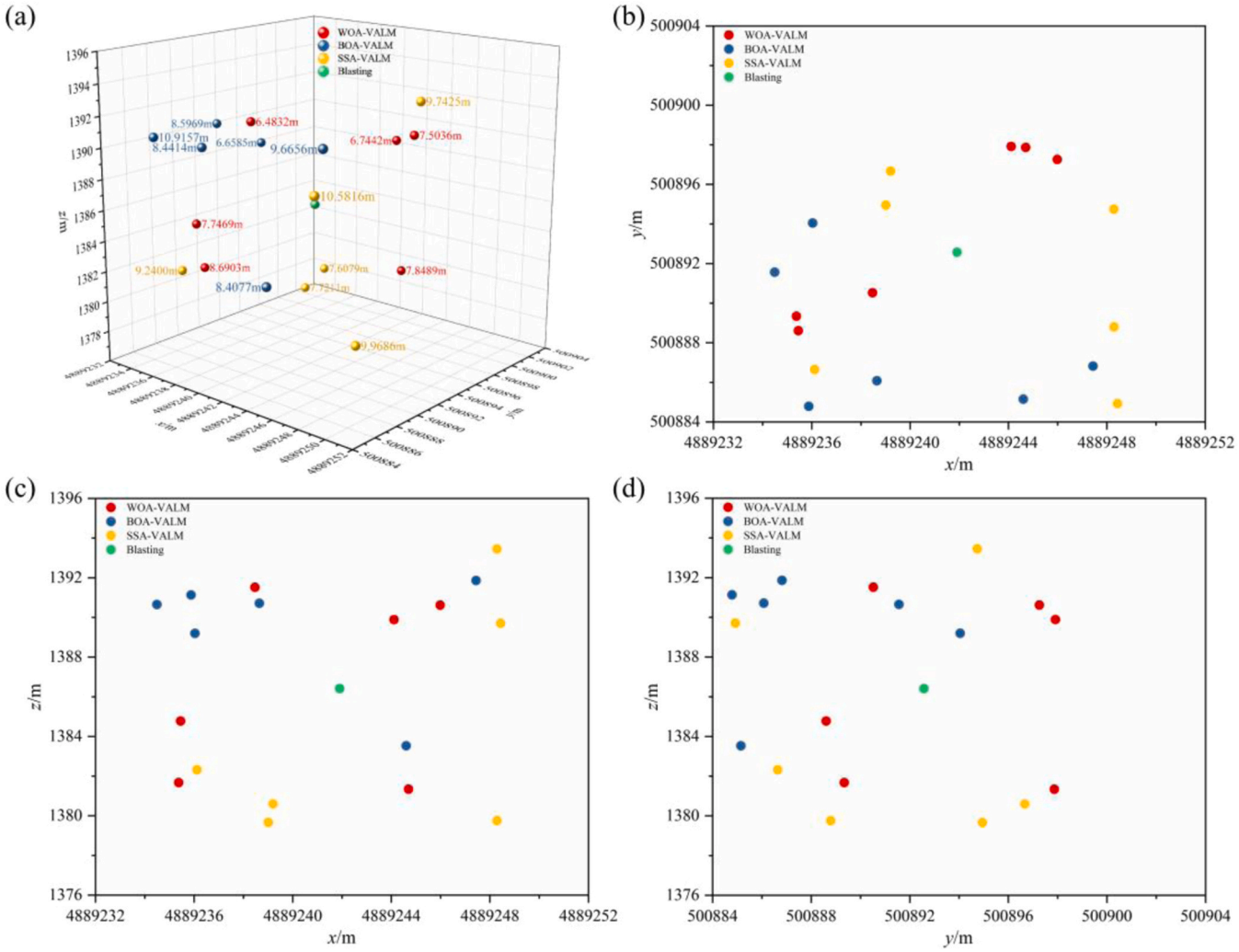


**Fig. 14.** Microseismic source location results for blasting case #3: (a) 3D visualization; (b) *x*-*y* plane projection; (c) *x*-*z* plane projection; (d) *y*-*z* plane projection. Numerical annotations in Fig. 14(a), such as 6.4832 m, represent location errors.

SSA, and then perform the global search within the given solution space to minimize the objective function. The searched optimal solution is the location of the microseismic source. The detailed procedure is described as follows (see Fig. 3):

(1) Determine the inversion boundaries of the source location $(x_0, y_0, z_0)$ and the P-wave velocity $(v_1, v_2, \ldots, v_n)$.
(2) Create the initial population in the given solution space, where each individual represents a set of potential inversion values $(x_0, y_0, z_0, v_1, v_2, \ldots, v_n)$.
(3) Calculate the value of the fitness function for all individuals in the population. The individual with the smallest fitness function value is regarded as the global best solution, and that with the largest fitness function value is regarded as the global worst solution.
(4) Update the positions of individuals and return to step (3). If no new global best solution appears, retain the original global best solution; otherwise, replace the original global best solution.
(5) If the maximum number of iterations is reached, output the current global best solution as the inversion result; otherwise, continue updating the positions of individuals through step (4).

## 3. Model validation

### 3.1. Data collection

Four blasting cases from a water diversion tunnel project in Xinjiang were selected to validate the microseismic source localization performance of WOA-VALM, BOA-VALM, and SSA-VALM. Related project overview can be found in Zhang et al. [40], and the blasting coordinates are listed in Table 1. To ensure the safety of the personnel and equipment, three microseismic monitoring sections were arranged, as shown in Fig. 4. The first monitoring section was located 80 m from the tunnel face, the second section 100 m, and the third section 120 m. For each monitoring section, one uniaxial accelerometer was installed on both the left and right spandrels to receive microseismic signals. Table 2 gives the sensor coordinates for these four blasting cases. Correspondingly, Fig. 5 (a)~(d) present microseismic signals monitored for these four blasting cases.

### 3.2. Determination of inversion boundaries

#### 3.2.1. Source location

The inversion boundaries for the source location should cover the microseismic development zone during the tunnel excavation process. If the inversion boundaries are too small, there may be no real solution within the inversion area, causing the objective function to fail to

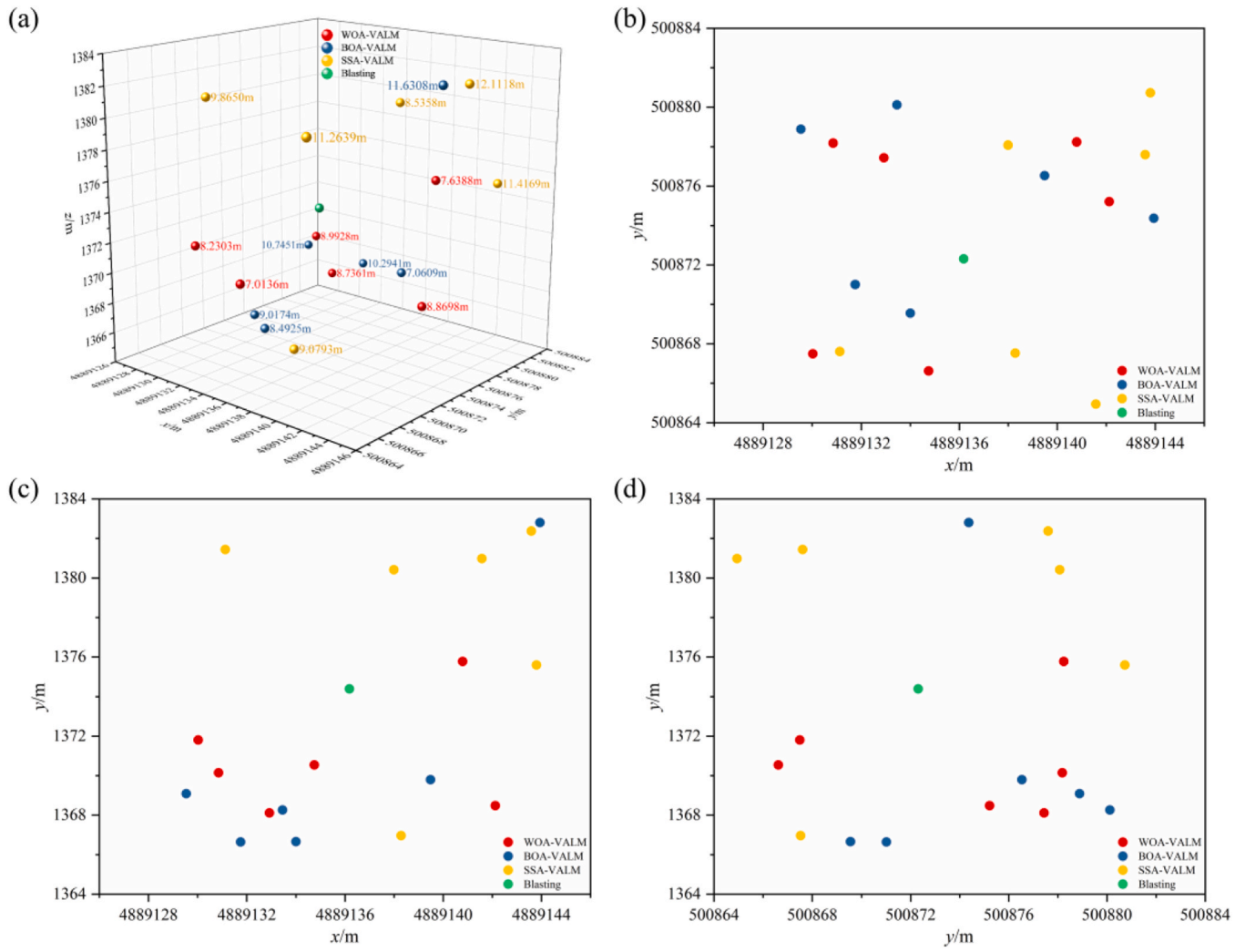


**Fig. 15.** Microseismic source location results for blasting case #4: (a) 3D visualization; (b) *x*-*y* plane projection; (c) *x*-*z* plane projection; (d) *y*-*z* plane projection. Numerical annotations in Fig. 15(a), such as 9.8650 m, represent location errors.

**Table 5**
Localization errors of the WOA-VALM, BOA-VALM, and SSA-VALM.

| Localization model | Localization error/m | Blasting case | | | |
|---|---|---|---|---|---|
| | | #1 | #2 | #3 | #4 |
| WOA-VALM | Minimum | 6.3931 | 4.8907 | 6.4832 | 7.0136 |
| | Maximum | 9.1282 | 7.7356 | 8.6903 | 8.9928 |
| | Average | 7.7021 | 6.0642 | 7.5028 | 8.2469 |
| BOA-VALM | Minimum | 7.0294 | 5.4347 | 6.6585 | 7.0609 |
| | Maximum | 10.5660 | 8.1248 | 10.9157 | 11.6308 |
| | Average | 8.4036 | 6.7998 | 8.7810 | 9.5401 |
| SSA-VALM | Minimum | 6.9376 | 5.5082 | 7.6079 | 8.5358 |
| | Maximum | 11.4388 | 9.1371 | 10.5816 | 12.1118 |
| | Average | 8.8558 | 7.3107 | 9.1436 | 10.3788 |

converge. On the other hand, if the inversion boundaries are too large, it will significantly increase the inversion cost. Therefore, determining the appropriate inversion boundaries for the source location is crucial for improving inversion accuracy and efficiency.

Along the x-axis (i.e., the excavation direction), the upper inversion boundary of the source location is set at the third monitoring section, and the lower inversion boundary is set 110 m in front of the first monitoring section, considering the following reasons: (1) The surrounding rock behind the third monitoring section has already been reinforced and returned to stability, meaning no new microseismic events are expected in that area; (2) The first monitoring section is located 80 m from the tunnel face, thus microseismic events within 30 m in front of the tunnel face can be localized. Along the y-axis (i.e., horizontal tunnel diameter) and the z-axis (i.e., vertical tunnel diameter), both the upper and lower inversion boundaries are set 30 m outside the tunnel perimeter, which is approximately 3.5–4.0 times the tunnel diameter. The inversion area for the source location is designed as a rectangular cuboid, as shown in Fig. 6. Based on these principles, Table 3 provides the inversion boundaries for the source location in the four blasting cases.

### 3.2.2. *P-wave velocity*

The WOA-VALM, BOA-VALM, and SSA-VALM treat the P-wave velocity as an inversion parameter without the need for prior measurement. To determine the inversion boundaries for the P-wave velocity, this study proposes a method that combines the true reflection tomography (TRT) technology. The TRT, as a geological prospecting method, is based on the physical principle that different media have different impedance to the propagation and attenuation of stress waves. By installing the seismic excitation system and sensors in surrounding rock, the TRT can obtain a wealth of spatial wavefield information.

Taking blasting case #1 as an example, Fig. 7 shows the relative P-wave velocity in the source location inversion area as measured by the TRT. To convert the relative P-wave velocity to the absolute P-wave velocity, first take a rock core at a known location and determine its

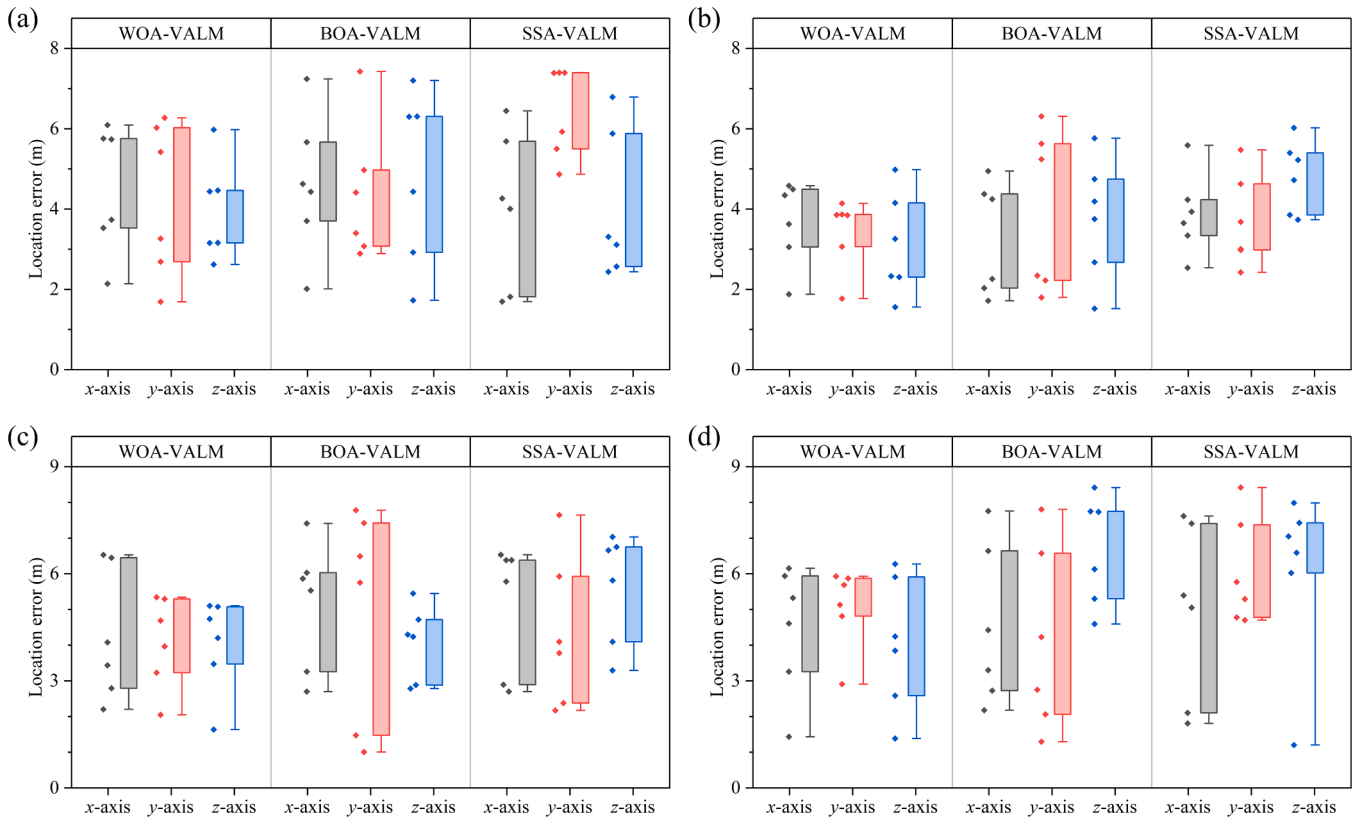


**Fig. 16.** Local location errors: (a) Blasting case #1; (b) Blasting case #2; (c) Blasting case #3; (d) Blasting case #4.

**Table 6**
Standard deviations of the localization errors of the WOA-VALM, BOA-VALM, and SSA-VALM.

| Localization model | Blasting case | | | |
|---|---|---|---|---|
| | #1 | #2 | #3 | #4 |
| WOA-VALM | 1.0183 m | 0.9607 m | 0.7308 m | 0.7159 m |
| BOA-VALM | 1.3511 m | 0.9971 m | 1.2995 m | 1.5225 m |
| SSA-VALM | 1.3406 m | 1.1165 m | 1.1179 m | 1.3047 m |

absolute P-wave velocity $v_a^*$, then calculate the ratio $\omega$ of absolute P-wave velocity $v_a^*$ to relative P-wave velocity $v_r^*$ at this location through Eq. (24), and finally multiply the relative P-wave velocity $v_r$ at other locations by the ratio $\omega$ through Eq. (25) to obtain the corresponding absolute P-wave velocity $v_a$. We take the maximum and minimum values of absolute P-wave velocity within the source location inversion area as the upper and lower inversion boundaries of P-wave velocity, respectively. According to the above principles, Table 4 gives the inversion boundaries for the P-wave velocity in the four blasting cases.

$$\omega = \frac{v_a^*}{v_r^*} \tag{24}$$

$$v_a = v_r \cdot \omega \tag{25}$$

### 3.3. Results analysis

After determining the inversion boundaries, the WOA-VALM, BOA-VALM, and SSA-VALM were used to conduct microseismic source localization. To test the stability of the solutions, the WOA-VALM, BOA-VALM, and SSA-VALM each performed six localization calculations for a single blasting case. For blasting case #1, the fitness function of the WOA-VALM converged to $2.30 \times 10^{-6}$, $2.91 \times 10^{-6}$, $1.99 \times 10^{-6}$, $3.24 \times 10^{-6}$, $1.14 \times 10^{-6}$, and $2.89 \times 10^{-6}$ at the 139th, 92nd, 125th, 186th, 101st, and 90th iterations respectively, as shown in Fig. 8(a). Similarly, Fig. 8(b)~(c) show the evolution process of the fitness function of the BOA-VALM and SSA-VALM, respectively. For blasting case #2, the evolution process of the fitness function of the WOA-VALM, BOA-VALM, and SSA-VALM is illustrated in Fig. 9(a)~(c), respectively. For blasting case #3, the evolution process of the fitness function of the WOA-VALM, BOA-VALM, and SSA-VALM is presented in Fig. 10 (a)~(c), respectively. For blasting case #4, the evolution process of the fitness function of the WOA-VALM, BOA-VALM, and SSA-VALM is displayed in Fig. 11(a)~(c), respectively.

Fig. 12 shows the microseismic source localization results for blasting case #1. Particularly, the localization error is calculated by Eq. (26). In the six localization calculations, the minimum localization error, maximum localization error, and average localization error of the WOA-VALM were 6.3931 m, 9.1282 m, and 7.7021 m, respectively. For the BOA-VALM, the minimum, maximum, and average localization errors were 7.0294 m, 10.5660 m, and 8.4036 m, respectively. For the SSA-VALM, the minimum, maximum, and average localization errors were 6.9376 m, 11.4388 m, and 8.8558 m, respectively. Compared to the BOA-VALM and SSA-VALM, the WOA-VALM had the smaller minimum, maximum, and average localization errors, indicating that the WOA-VALM attained the highest localization accuracy among these three models.

$$error_g = \sqrt{(x_p - x_r)^2 + (y_p - y_r)^2 + (z_p - z_r)^2} \tag{26}$$

where, $(x_p, y_p, z_p)$ is the predicted source location of the location model; $(x_r, y_r, z_r)$ is the real source location.

Figs. 13, 14 and 15 illustrate the microseismic source localization results for blasting cases #2, #3, and #4, respectively. Similarly, the WOA-VALM achieved the superior localization accuracy in comparison with the BOA-VALM and SSA-VALM. For the above three blasting cases,


**Fig. 17.** Comparative analysis with traditional microseismic source location models.

the minimum localization errors of the WOA-VALM were 4.8907 m, 6.4832 m, and 7.0136 m, the maximum localization errors were 7.7356 m, 8.6903 m, and 8.9928 m, and the average localization errors were 6.0642 m, 7.5028 m, and 8.2469 m, respectively, all of which were lower than those of the BOA-VALM and SSA-VALM, as detailed in Table 5.

Next, we analyzed the local localization errors of the WOA-VALM, BOA-VALM, and SSA-VALM along the $x$-axis, $y$-axis, and $z$-axis through Eq. (27). Referring to Fig. 16(a), for blasting case #1, the WOA-VALM's local localization errors along the $x$-axis, $y$-axis, and $z$-axis were all controlled within 6.3 m, while those of the BOA-VALM and SSA-VALM in these three directions reached 7.3 m or more. Compared to the BOA-VALM and SSA-VALM, the WOA-VALM achieved the better control over local localization errors. This advantage of the WOA-VALM

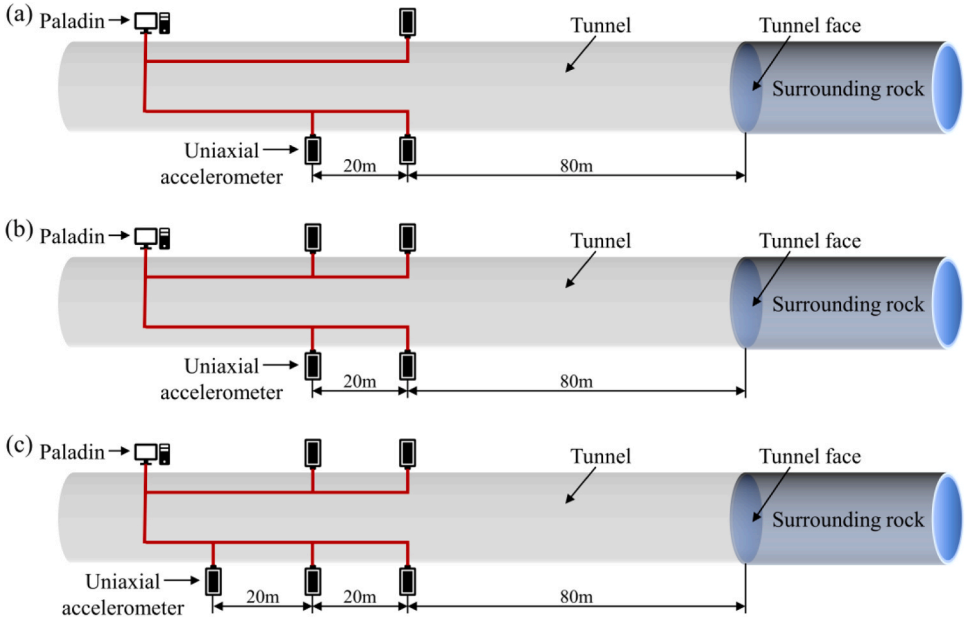


**Fig. 18.** Sensor layout: (a) Three sensors; (b) Four sensors; (c) Five sensors.

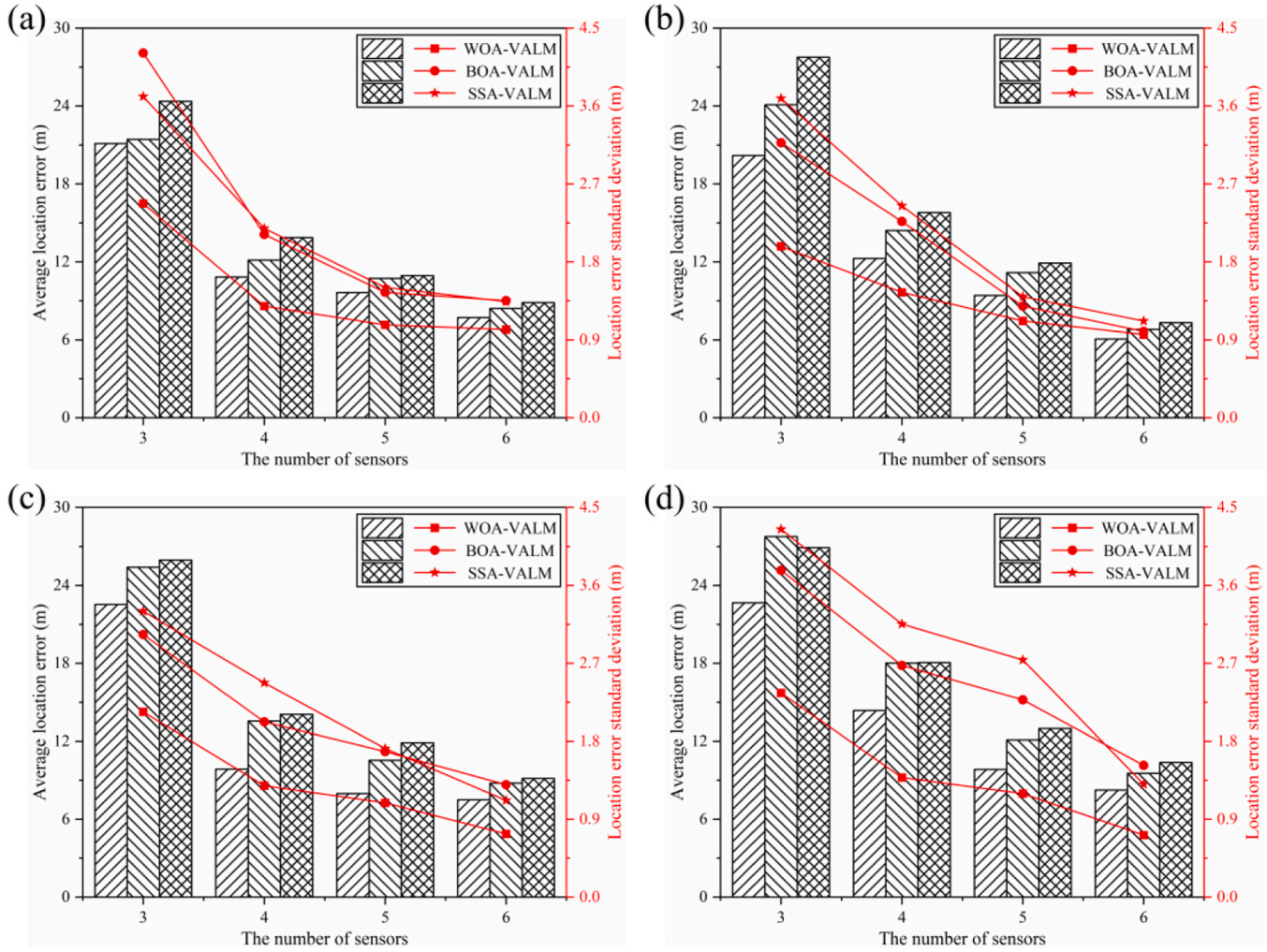


**Fig. 19.** Influence of the number of sensors on microseismic source location: (a) Blasting case #1; (b) Blasting case #2; (c) Blasting case #3; (d) Blasting case #4.

can also be found for blasting cases #2 (Fig. 16(b)), #3 (Fig. 16(c)), and #4 (Fig. 16(d)).

$$error_l = \begin{cases} |x_p - x_r| & along\ the\ x-axis \\ |y_p - y_r| & along\ the\ y-axis \\ |z_p - z_r| & along\ the\ z-axis \end{cases} \quad (27)$$

where, $(x_p, y_p, z_p)$ is the predicted source location of the location model; $(x_r, y_r, z_r)$ is the real source location.

Finally, we calculated the standard deviations of the localization errors in the six microseismic source localization calculations for the WOA-VALM, BOA-VALM, and SSA-VALM, as summarized in Table 6. For blasting cases #1, #2, #3, and #4, the WOA-VALM achieved the standard deviations of the localization errors of 1.0183 m, 0.9607 m, 0.7308 m, and 0.7159 m, respectively, which are lower than those of the BOA-VALM and SSA-VALM. Consequently, the WOA-VALM achieved the better solution stability compared to the BOA-VALM and SSA-VALM.

## 4. Discussion

### 4.1. Comparison with traditional microseismic source localization models

The Gauss-Newton algorithm (GNA) and simplex algorithm (SA) are commonly used to solve traditional microseismic source localization models. This section presents a comparative analysis of the WOA-VALM, BOA-VALM, and SSA-VALM with the GNA-PTLM, SA-PTLM, GNA-PVLM, SA-PVLM, GNA-PLM, and SA-PLM in terms of localization accuracy, solution stability, and localization efficiency. Particularly, the localization accuracy, solution stability, and localization efficiency are measured by the average localization error, the standard deviation of localization errors, and the average convergence time over six localization calculations, respectively.

As illustrated in Fig. 17, the WOA-VALM, BOA-VALM, and SSA-VALM offer certain advantages over traditional microseismic source localization models in terms of localization accuracy, solution stability, and localization efficiency. Among these nine models, the WOA-VALM achieved the smallest average localization error, the lowest standard deviation of localization errors, and the shortest average convergence time, making it the most optimal in terms of localization performance. Taking blasting case #1 as an example, compared to the GNA-PTLM, SA-PTLM, GNA-PVLM, SA-PVLM, GNA-PLM, and SA-PLM, the WOA-VALM reduced the average localization error by 30.00 %, 24.69 %, 40.01 %, 37.48 %, 40.18 %, and 30.30 %, respectively. Additionally, the standard deviation of localization errors was decreased by 35.73 %, 42.42 %, 65.15 %, 55.10 %, 58.68 %, and 50.37 %, respectively, and the average convergence time was shortened by 55.29 %, 49.25 %, 52.66 %, 54.20 %, 49.70 %, and 48.32 %, respectively.

### 4.2. Influence of sensor quantity on localization performance

In practical engineering applications, due to the complexity of both internal and external environments, it is difficult to ensure that all sensors function properly or are successfully triggered. Therefore, it is necessary to discuss the impact of the number of sensors on the localization performance of the WOA-VALM, BOA-VALM, and SSA-VALM. In this Section, three additional microseismic source location experiments were conducted. In these experiments, the number of sensors was reduced from the original 6–3, 4, and 5, respectively. The sensor layout for these experiments is shown in Fig. 18.

Fig. 19 shows the microseismic source localization results with different numbers of sensors. It can be observed that as the number of sensors involved in microseismic source location increases, the localization accuracy and solution stability of the WOA-VALM, BOA-VALM, and SSA-VALM improve accordingly. Taking blasting case #1 as an example, with only 3 sensors, the average localization errors for the WOA-VALM, BOA-VALM, and SSA-VALM were 21.12 m, 21.44 m, and 24.36 m, respectively, and the standard deviations of localization errors were 2.47 m, 4.21 m, and 3.71 m, respectively. However, when the number of sensors was increased to 4, 5, and 6, the WOA-VALM's average localization error decreased by 48.75 %, 54.41 %, and 63.53 %, respectively, and meanwhile the standard deviation of localization errors decreased by 47.94 %, 56.72 %, and 58.85 %, respectively. Similarly, these laws can be found for the BOA-VALM and SSA-VALM. In order to meet the field application requirements, we recommend using at least 4 sensors for microseismic source location with the WOA-VALM, BOA-VALM, and SSA-VALM. Additionally, when field conditions allow, it is advisable to deploy as many backup sensors as possible to enhance the resilience of the microseismic monitoring network and prevent significant degradation in localization performance due to sensor failure.

## 5. Conclusion

This study proposed a novel microseismic source localization model that considers the anisotropy of P-wave velocity. The model assigns a unique P-wave velocity to each propagation path, abandoning the assumption of a homogeneous velocity field. Besides, it treats the P-wave velocity as a co-inversion parameter along with the source location, solving the technical challenge of inaccurate P-wave velocity measurements. To solve this model, we designed three parameter inversion schemes based on metaheuristic multi-objective optimization algorithms, including the WOA, BOA, and SSA.

To test the localization performance of the model, we collected four blasting cases from a water diversion tunnel project in Xinjiang, China. The results revealed that the WOA-VALM achieved the superior localization accuracy and efficiency for these four blasting cases in comparison with the BOA-VALM and SSA-VALM, with the smallest overall localization error, local localization error, and average convergence time. Then, by analyzing the standard deviation of localization errors from six microseismic source localization calculations, it was evident that the WOA-VALM had the greater solution stability than the BOA-VALM and SSA-VALM. Moreover, we compared the proposed model with traditional models, demonstrating that the proposed model had advantages in terms of localization accuracy, localization efficiency, and solution stability.

Finally, we discussed the impact of the number of sensors on microseismic source localization. The results indicate that the localization performance of the WOA-VALM, BOA-VALM, and SSA-VALM is closely related to the number of sensors used. As the number of sensors increases, the localization performance of the models improve. For field applications, we recommend using at least 4 sensors for localization, and, where possible, deploying additional sensors to strengthen the resilience of the microseismic monitoring network.

## Funding

This research is supported by the National Natural Science Foundation of China under Grant Nos. 42472351, 42177140, 52404127, and 42207235, the Natural Science Foundation of Hubei Province under Grant No. 2024AFD359, the Young Elite Scientist Sponsorship Program by CAST under Grant No. YESS20230742, and the China Postdoctoral Science Foundation Program under Grant No. 2024T170684. These supports are gratefully acknowledged.

## CRediT authorship contribution statement

**Yin Xin:** Writing – review & editing, Writing – original draft, Methodology, Investigation, Conceptualization. **Gao Feng:** Writing – review & editing, Writing – original draft, Investigation. **Yu Honggan:** Writing – review & editing, Writing – original draft, Methodology, Investigation. **Pan Yucong:** Writing – review & editing, Investigation. **Liu Quansheng:** Writing – review & editing, Investigation. **Liu He:** Writing – review & editing, Investigation.

## Declaration of Competing Interest

The authors declare that they have no known competing financial interests or personal relationships that could have appeared to influence the work reported in this paper.

## References


[1] M. Askaripour, A. Saeidi, A. Rouleau, P. Mercier-Langevin, Rockburst in underground excavations: a review of mechanism, classification, and prediction methods, Undergr. Space 7 (2022) 577–607.
[2] E. Blias, V. Grechka, Analytic solutions to the joint estimation of microseismic event locations and effective velocity model, Geophysics 78 (2013) KS51–KS61.
[3] R. Buland, Mechanics of locating earthquakes, B. Seismol. Soc. Am. 66 (1976) 173–187.
[4] S. Cheng, X. Yin, F. Gao, Y. Pan, Microseismic data-driven short-term rockburst evaluation in underground engineering with strategic data augmentation and extremely randomized forest, Mathematics (2024).
[5] S. Cheng, X. Yin, F. Gao, Y. Pan, Surrounding rock squeezing classification in underground engineering using a hybrid paradigm of generative artificial intelligence and deep ensemble learning, Mathematics (2024).
[6] W. Choi, W. Kim, S. Pyun, A simple inversion algorithm to estimate a linearly increasing velocity model for microseismic monitoring, Explor. Geophys. 49 (2018) 647–654.
[7] F. Dai, L. Guo, N.W. Xu, Y.L. Fan, J. Xu, P. Jiang, Improvement of microseismic location based on an anisotropic velocity model, Chin. J. Geophys.-Chin. Ed. 59 (2016) 3291–3301.
[8] L.J. Dong, X.B. Li, Z.L. Zhou, G.H. Chen, J. Ma, Three-dimensional analytical solution of acoustic emission source location for cuboid monitoring network without pre-measured wave velocity, Trans. Nonferrous Met. Soc. China 25 (2015) 293–302.
[9] L.J. Dong, D.Y. Sun, X.B. Li, K. Du, Theoretical and experimental studies of localization methodology for AE and microseismic sources without pre-measured wave velocity in mines, IEEE Access 5 (2017) 16818–16828.
[10] L.J. Dong, W. Zou, X.B. Li, W.W. Shu, Z.W. Wang, Collaborative localization method using analytical and iterative solutions for microseismic/acoustic emission sources in the rockmass structure for underground mining, Eng. Fract. Mech. 210 (2019) 95–112.
[11] Geiger L., (1912). Probability Method for the Determination of Earthquake Epicentres from the Arrival Time only. Bull. St. Louis Univ. 8, 60.
[12] F.S. Gharehchopogh, H. Gholizadeh, A comprehensive survey: whale optimization algorithm and its applications, SWARM Evolut. Comput. 48 (2019) 1–24.
[13] S.Y. Gong, L.M. Dou, X.P. Ma, Z.L. Mu, H. He, J. He, Study on the construction and solution technique of anisotropic velocity model in the location of coal mine tremor, Chin. J. Geophys.-Chin. Ed. 55 (2012) 1757–1763.
[14] G.J. Huang, J. Ba, Q.Z. Du, J.M. Carcione, Simultaneous inversion for velocity model and microseismic sources in layered anisotropic media, J. Pet. Sci. Eng. 173 (2019) 1453–1463.
[15] Inglada, V., (1928). The Calculation of the Stove Coordinates of A Nahbebens. Gerlands Beitrage Zur Geophys 19, 73-98.
[16] Leighton, F., Blake, W., 1970. Rock Noise Source Location Techniques. US Department of Interior, Bureau of Mines.
[17] Leighton, F., Duvall, W.I., 1972. A Least Squares Method for Improving the Source Location of Rock Noise. US Department of Interior, Bureau of Mines.
[18] N. Li, M.C. Ge, E.Y. Wang, Two types of multiple solutions for microseismic source location based on arrival-time-difference approach, Nat. Hazard. 73 (2014) 829–847.
[19] X.B. Li, Z.W. Wang, L.J. Dong, Locating single-point sources from arrival times containing large picking errors (LPEs): the virtual field optimization method (VFOM), Sci. Rep. 6 (2016).
[20] F. Liu, T.H. Ma, C.A. Tang, F. Chen, Prediction of rockburst in tunnels at the Jinping II hydropower station using microseismic monitoring technique, Tunn. Undergr. Space Technol. 81 (2018) 480–493.
[21] L. Liu, S.J. Li, Y.X. Xiao, S.J. Chen, Z.F. Wang, G.L. Feng, Y. Wang, An inverted heterogeneous velocity model for microseismic source location in deep buried tunnels, Rock. Mech. Rock. Eng. 56 (2023) 4855–4880.
[22] C.C. Ma, Y.P. Jiang, T.B. Li, Gravitational search algorithm for microseismic source location in tunneling: performance analysis and engineering case study, Rock. Mech. Rock. Eng. 52 (2019) 3999–4016.
[23] S.N. Makhadmeh, M.A. Al-Betar, A.K. Abasi, M.A. Awadallah, I. Abu Doush, Z.A. A. Alyasseri, O.A. Alomari, Recent advances in butterfly optimization algorithm, its versions and applications, Arch. Comput. Methods Eng. 30 (2023) 1399–1420.
[24] H. Shi, L.X. Pang, R.Y. Shi, Solution of microseismic monitoring non-linear location equations based matlab, Adv. Struct. Eng. PTS 1-3 (2011) 1628.
[25] S.B. Tang, Y.H. Liu, H.R. Xu, X.M. Chen, Review for the microseismic source location in surrounding rock of deep-buried tunnel, J. Cent. South Univ. 30 (2023) 4182–4196.
[26] C.H. Thurber, Nonlinear earthquake location - theory and examples, B. Seismol. Soc. Am. 75 (1985) 779–790.
[27] S. Wang, S. Yu, X. Hu, B. Yang, Effects of folded fissure properties on tunnel model failure: experiments and numerical simulations, Eng. Fract. Mech. 310 (2024) 110487.
[28] J. Wu, Q.S. Liu, X.P. Zhang, C.Y. Zhou, X. Yin, W.Q. Xie, X. Liang, J.Q. Huang, Attenuation characteristics of impact-induced seismic wave in deep tunnels: an in situ investigation based on pendulum impact test, J. Rock. Mech. Geotec. Eng. 14 (2022) 494–504.
[29] Xiang, Z., Yu, S., Wang, X., 2024. Modeling the Hydraulic Fracturing Processes in Shale Formations Using a Meshless Method, Water.
[30] J.K. Xue, B. Shen, A survey on sparrow search algorithms and their applications, Int. J. Syst. Sci. 55 (2024) 814–832.
[31] X. Yin, S. Cheng, H. Yu, Y. Pan, Q. Liu, X. Huang, F. Gao, G. Jing, Probabilistic assessment of rockburst risk in TBM-excavated tunnels with multi-source data fusion, Tunn. Undergr. Space Technol. 152 (2024) 105915.
[32] X. Yin, Q. Liu, X. Huang, Y. Pan, Real-time prediction of rockburst intensity using an integrated CNN-Adam-BO algorithm based on microseismic data and its engineering application, Tunn. Undergr. Space Technol. 117 (2021) 104133.
[33] X. Yin, Q. Liu, J. Lei, Y. Pan, X. Huang, Y. Lei, Hybrid deep learning-based identification of microseismic events in TBM tunnelling, Measurement 238 (2024) 115381.
[34] X. Yin, Q.S. Liu, X. Huang, Y.C. Pan, Development and application of a novel hybrid CEEMDAN-LWT denoising approach in microseismic monitoring, Pure Appl. Geophys. 179 (2022) 3279–3294.
[35] X. Yin, Q.S. Liu, Y.C. Pan, X. Huang, J. Wu, X.Y. Wang, Strength of stacking technique of ensemble learning in rockburst prediction with imbalanced data: comparison of eight single and ensemble models, Nat. Resour. Res. 30 (2021) 1795–1815.
[36] S. Yu, X. Hu, Z. Liang, Exploring the elliptic fissure cracking mechanisms from the perspective of sand 3D printing technology and Meshfree numerical strategy, Int. J. Solids Struct. 310 (2025) 113216.
[37] S. Yu, X. Ren, J. Zhang, Using an improved SPH algorithm to simulate thermo-hydro-mechanical-damage coupling problems in rock masses, Case Stud. Therm. Eng. 47 (2023) 103085.
[38] S. Yu, X. Ren, J. Zhang, Z. Sun, Simulating the chemical-mechanical-damage coupling problems of cement-based materials using an improved smoothed particle hydrodynamics method, Case Stud. Constr. Mater. 18 (2023) e02018.
[39] Yu, S., Yang, X., Ren, X., Zhang, J., Gao, Y., Zhang, T., 2023c. Shear Damage Simulations of Rock Masses Containing Fissure-Holes Using an Improved SPH Method, Materials.
[40] Q. Zhang, X.P. Zhang, Q.S. Liu, J.B. Qiu, J. Wu, Rockburst prediction and prevention in a deep-buried tunnel excavated by drilling and blasting: a case study, Eng. Geol. 330 (2024).
[41] S.C. Zhang, C.A. Tang, Y.C. Wang, J.M. Li, T.H. Ma, K.K. Wang, Review on early warning methods for rockbursts in tunnel engineering based on microseismic monitoring, Appl. Sci.-BASEL 11 (2021).
[42] J. Zhou, X.B. Li, H.S. Mitri, Evaluation method of rockburst: state-of-the-art literature review, Tunn. Undergr. Space Technol. 81 (2018) 632–659.
[43] J. Zhou, X.J. Shen, Y.G. Qiu, X.Z. Shi, M. Khandelwal, Cross-correlation stacking-based microseismic source location using three metaheuristic optimization algorithms, Tunn. Undergr. Space Technol. 126 (2022).
[44] S.T. Zhou, Z.X. Zhang, X.D. Luo, S.S. Niu, N. Jiang, Y.K. Yao, Developing a hybrid CEEMDAN-PE-HE-SWT method to remove the noise of measured carbon dioxide blast wave, Measurement 223 (2023).


**Xin Yin** received his PhD from Wuhan University, Wuhan, China. His research focuses on numerical modeling and digital twin in geotechnical engineering.